VIP **Bioimaging** *Very Important Paper*

DOI: 10.1002/anie.201407420

Epitaxial Seeded Growth of Rare-Earth Nanocrystals with Efficient 800 nm Near-Infrared to 1525 nm Short-Wavelength Infrared Downconversion Photoluminescence for In Vivo Bioimaging**

*Rui Wang, Xiaomin Li, Lei Zhou, and Fan Zhang**

Abstract: *Novel β-$NaGdF_4$/Na(Gd,Yb)F_4:Er/$NaYF_4$:Yb/$NaNdF_4$:Yb core/shell1/shell2/shell3 (C/S1/S2/S3) multi-shell nanocrystals (NCs) have been synthesized and used as probes for in vivo imaging. They can be excited by near-infrared (800 nm) radiation and emit short-wavelength infrared (SWIR, 1525 nm) radiation. Excitation at 800 nm falls into the "biological transparency window", which features low absorption by water and low heat generation and is considered to be the ideal excitation wavelength with the least impact on biological tissues. After coating with phospholipids, the water-soluble NCs showed good biocompatibility and low toxicity. With efficient SWIR emission at 1525 nm, the probe is detectable in tissues at depths of up to 18 mm with a low detection threshold concentration (5 nM for the stomach of nude mice and 100 nM for the stomach of SD rats). These results highlight the potential of the probe for the in vivo monitoring of areas that are otherwise difficult to analyze.*

The past decade has witnessed an explosion in the investigation of novel biomedical imaging methods for the early detection and diagnosis of diseased tissues. Among them, tomographic imaging techniques, such as computed tomography (CT), positron emission tomography (PET), and magnetic resonance imaging (MRI), play an important role because of their superiority in terms of unlimited penetration depth.[1] However, they still suffer from some inevitable drawbacks, such as limited spatial resolution and an inability to visualize real-time dynamics owing to long image acquisition times.[2] In comparison, photoluminescence (PL)-based biomedical imaging has the advantages of fast feedback, high sensitivity, and high resolution, but is limited by a low tissue-penetration depth.[3] Typically, fluorophores that emit in the visible range (400–750 nm) can only penetrate approximately 1 mm into the tissue because of the absorption and scattering of the photons,[3,4] and for those emitting in the first near-infrared (NIR-I) window (750–900 nm), which has been named the "biological transparency window", the penetration depth merely reaches several millimeters.[5,6] Thus, a new imaging method that features high spatial resolution, fast feedback, and deep tissue penetration is desired to optimize the accuracy and sensitivity of PL-based biomedical imaging.

Recently, optical simulations have led to predictions of a second "tissue-transparent window" with short-wavelength infrared light (SWIR, 1000–2300 nm), which features lower tissue autofluorescence than the NIR-I window and up to a 1000-fold reduction in scattering losses, enabling unprecedented improvements in detection depth and resolution.[7] Thus far, several kinds of materials that are capable of generating SWIR PL have been reported, such as SWIR quantum dots (QDs)[8] and single-walled carbon nanotubes (SWNTs).[9,10] However, SWIR QDs always contain toxic elements, such as mercury, lead, or arsenic,[11] which are undesirable in biomedical applications.[7,12] SWIR Ag_2S QDs feature low toxicity, but suffer from serious quenching by both air and irradiation.[3] Although SWNTs have revealed good performance in SWIR biomedical imaging, there are several drawbacks that cannot be ignored before their widespread application as SWIR imaging agents, such as optimal excitation outside the NIR–SWIR windows of transparency near 650 nm and broad length distributions spanning hundreds of nanometers.[13] Hence, the design of novel materials for SWIR biomedical imaging is an urgent task.

Lanthanide ions (Lns) are spectroscopically complex species, a quality that facilitates the use of their optical modes in a wide spectral window, which is not possible with SWNTs. Compared with the previously reported handful of SWIR organic dyes and QDs, lanthanide-based luminescent materials have many advantages, including high efficiency, low photo-bleaching, long luminescence lifetimes, and low long-term cytotoxicity. Up to now, Sm^{3+}, Dy^{3+}, Ho^{3+}, Pr^{3+}, Yb^{3+}, Nd^{3+}, Er^{3+}, and Tm^{3+} based complexes and nanomaterials have been reported and exploited as SWIR imaging probes with an emission range of 1000–1600 nm.[1,14] However, as most of these lanthanide-based SWIR probes have high molar excitation coefficients under UV irradiation or at 488, 514, and 532 nm, the tissue penetration depth is seriously limited owing to the strong absorption and scattering of photons in these excitation ranges.[15,16] Although lanthanide-based probes with Yb^{3+} either as the luminescence center or as the sensitizer can be excited by 980 nm light for SWIR emission,[7,17] the water in biological structures would overwhelmingly attenuate 980 nm light, and transform its energy into local heat, which could induce heat damage in cells and tissues.[18–21] Therefore, it is essential for efficient bioimaging

---

[*] R. Wang, X. M. Li, L. Zhou, Prof. Dr. F. Zhang
Department of Chemistry, Laboratory of Advanced Materials
Fudan University
Shanghai 200433 (P.R. China)
E-mail: zhang_fan@fudan.edu.cn

[**] The work was supported by the NSFC (21322508, 21101029, 21273041, and 21210004), the China National Key Basic Research Program (973 Project; 2013CB934100, 2012CB224805, and 2010CB933901), the Shanghai Rising-Star Program (12A1400400), the Program for New Century Excellent Talents in University (NCET), and the State Key Laboratory of Pollution Control and Resource Reuse Foundation (PCRRF12001).

Supporting information for this article is available on the WWW under http://dx.doi.org/10.1002/anie.201407420.

to develop a novel lanthanide-based SWIR probe with an optimized excitation wavelength.

Herein, we fabricated a novel kind of β-$NaGdF_4$/Na(Gd,Yb)F_4:Er/$NaYF_4$:Yb/$NaNdF_4$:Yb core/shell 1/shell 2/shell 3 (C/S1/S2/S3) multi-shell nanocrystals (NCs) as an efficient 800 nm NIR to 1525 nm SWIR probe for in vivo bioimaging. Excitation at 800 nm is located in the biological transparency window (Supporting Information, Figure S1) with low absorption by water and heat generation, and is considered to be the ideal excitation wavelength with the least impact on biological tissues.[18,22] With efficient SWIR emission at 1525 nm, the probe is detectable in deep tissues up to 18 mm with a low detection threshold concentration (5 nM for the stomach of nude mice and 100 nM for the stomach of Sprague–Dawley (SD) rats). These results highlight the potential of the probe for the specific detection and therapy monitoring of areas that are otherwise difficult to detect.

C/S1/S2/S3 β-$NaGdF_4$/Na(Gd,Yb)F_4:Er/$NaYF_4$:Yb/$NaNdF_4$:Yb NCs were synthesized by epitaxial seeded growth, and are composed of the $NaGdF_4$ core (the seed for epitaxial growth), a Na(Gd,Yb)F_4:Er shell (S1; the SWIR PL layer), a $NaYF_4$:Yb shell (S2; the energy transfer layer), and a $NaNdF_4$:Yb shell (S3; the energy absorption layer; Scheme 1). After absorption of 800 nm light (Nd^{3+}, $^4I_{9/2}\rightarrow{}^4F_{5/2}$), the S3 shell transfers its energy to the inner layer S2 ($Nd^{3+}\rightarrow Yb^{3+}$, $^2F_{7/2}\rightarrow{}^2F_{5/2}$). Energy is transferred within this layer by the co-doped Yb^{3+} until the Er^{3+} in the S1 shell is sensitized ($Yb^{3+}\rightarrow Er^{3+}$, $^4I_{15/2}\rightarrow{}^4I_{11/2}$). This results in relaxation from the excited state of Er^{3+} through the release of a 1525 nm ($^4I_{13/2}\rightarrow{}^4I_{15/2}$) photon along with phonon vibration.

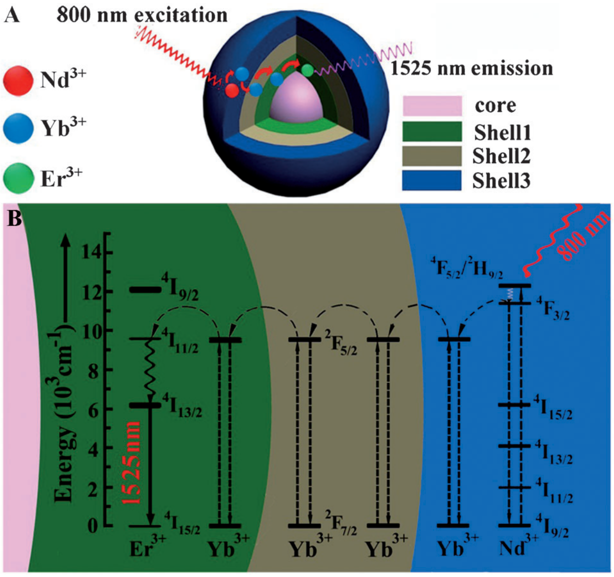

Scheme 1. A) Structure of the C/S1/S2/S3 NCs for 1525 nm luminescence. B) Proposed energy transfer mechanisms in the multi-layer core/shell NCs.

Images of the NCs before and after growth of the S1, S2, and S3 shells show that the nearly monodispersed and uniform $NaGdF_4$ cores with an average diameter of 5.94 ± 0.37 nm are gradually grown into core/shell NCs with diameters of 8.27 ± 0.33, 10.47 ± 0.47, and 11.79 ± 0.77 nm with very narrow size distributions ($\sigma < 10\%$) after the successive epitaxial growth of the Na(Gd,Yb)F_4:Er, $NaYF_4$:Yb, and $NaNdF_4$:Yb layers, respectively (Figure 1 A–D). High-resolution TEM (HRTEM) demonstrates that the resultant C/S1/S2/S3 NCs are highly crystalline and maintain the hexagonal crystal structure of the initial $NaGdF_4$ core (Figure 1 E). The d-space of the lattice planes measured from the HRTEM image is approximately 3.20 Å and corresponds to the lattice parameters of the (110) planes of β-phase $NaNdF_4$. The selected area electron diffraction (SAED) pattern of the resultant C/S1/S2/S3 NCs also confirms the highly crystalline nature of the material with a hexagonal crystal structure (Figure 1 F). In the X-ray diffraction (XRD) patterns (Figure S2), small shifts of the (110) and (101) diffraction peaks can also be detected because of the small lattice mismatch (ca. 3.5 %) between β-$NaGdF_4$ and β-$NaYbF_4$ (Table S1). The energy-dispersive X-ray (EDX) pattern (Figure S3) confirmed the presence of Na, F, Gd, Yb, Y, and Nd in the C/S1/S2/S3 NCs. XPS spectra (Figure S4) of the C/S1/S2/S3 NCs under argon ion bombard-

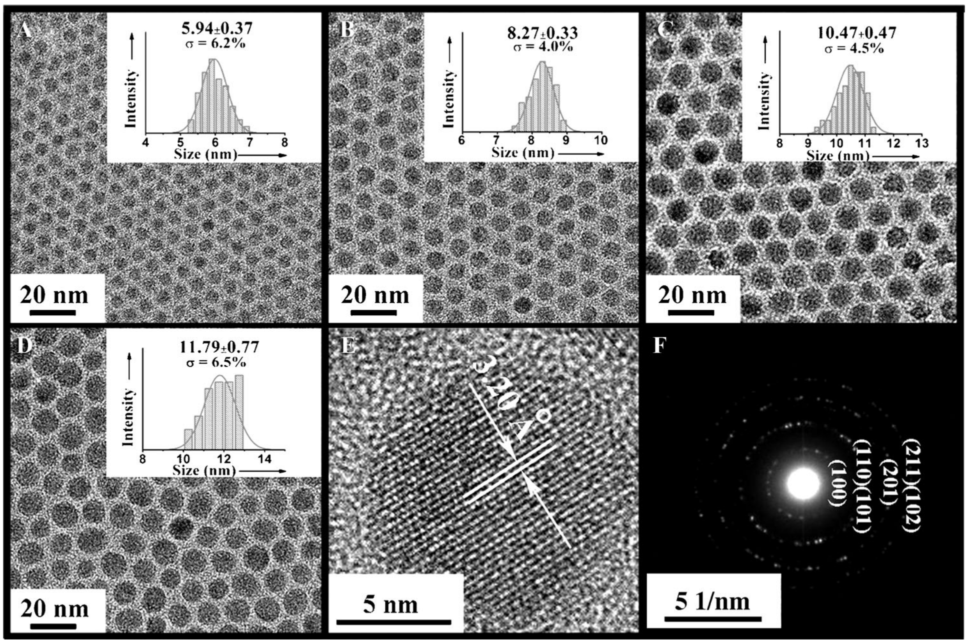

Figure 1. A–D) TEM images and size distributions of the $NaGdF_4$ core (A), $NaGdF_4$/$NaYbF_4$:Er (B), $NaGdF_4$/$NaYbF_4$:Er/$NaYF_4$:Yb (C), and $NaGdF_4$/$NaYbF_4$:Er/$NaYF_4$:Yb/$NaNdF_4$:Yb (D) NCs. E) HRTEM image and F) SAED pattern of the C/S1/S2/S3 NCs.

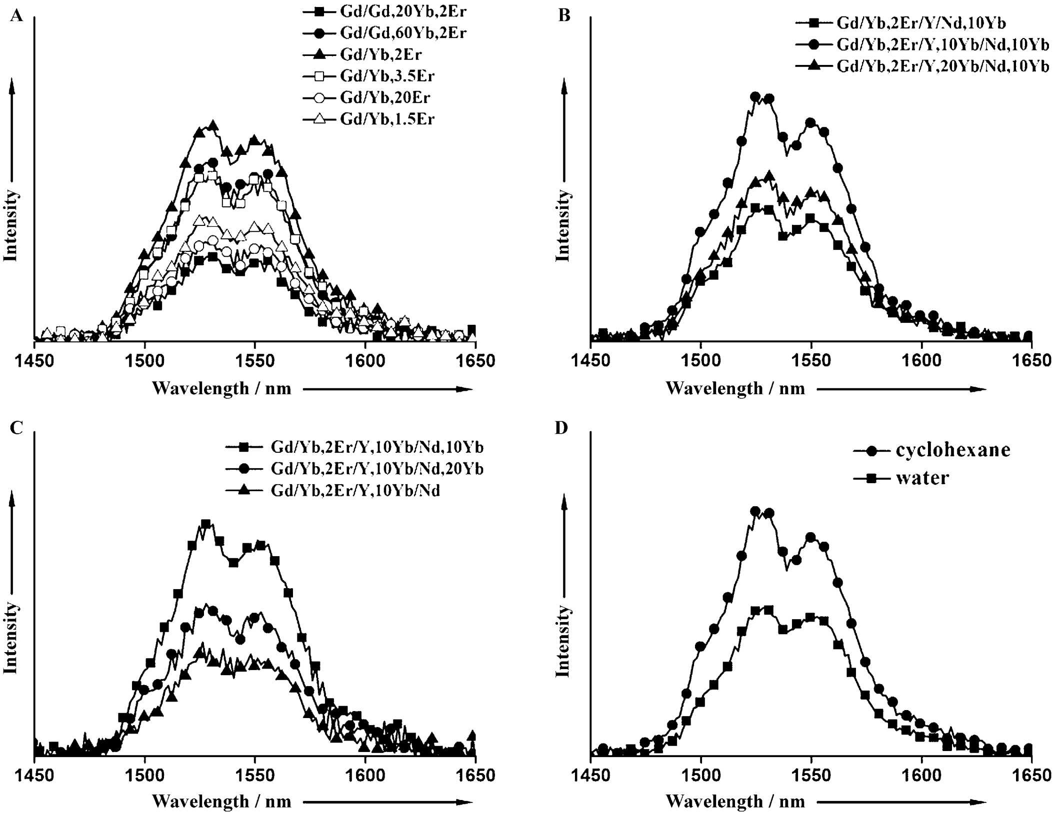

Figure 2. SWIR emission spectra of A) $NaGdF_4/Na(Gd,Yb)F_4$:Er NCs with various Yb/Er ratios, B) $NaGdF_4/NaYbF_4$:Er/$NaYF_4$:xYb/$NaNdF_4$:Yb ($x=0$, 10, and 20%) NCs, C) $NaGdF_4/NaYbF_4$:Er/$NaYF_4$:Yb/$NaNdF_4$:xYb ($x=0$, 10, and 20%) NCs, and D) $NaGdF_4/NaYbF_4$:2Er/$NaYF_4$:10Yb/$NaNdF_4$:10Yb NCs dispersed in cyclohexane (●) and water (■). The emission spectra in (A) were obtained under 980 nm excitation (20 W cm^{-2}), whereas the emission spectra in (B)–(D) were obtained under 800 nm excitation (20 W cm^{-2}).

ment with different bombardment times (0, 20, 50, 70, 100 s) further demonstrated the multilayer core/shell nanostructure with different components. Before etching, only Nd^{3+} (3d), Y^{3+} (3d, 3p), and weak Yb^{3+} (4d) signals could be detected for the S3 and S2 layers. Further etching for 20 to 100 s led to a gradual increase in intensity of the Yb^{3+} 4d and Gd^{3+} 3d signals from the S1 layer and the core of the NCs, respectively. As the 1525 nm SWIR PL occurs following the resonant transfer of excitation energy from the Yb sensitizer to the Er activator, efficient resonant energy transfer theoretically requires a high concentration of the Yb sensitizer. Therefore, to realize highly efficient 1525 nm SWIR PL, we needed to find the optimal doping concentration for the Yb sensitizer. In our case, the doping ratio of Yb^{3+} and Er^{3+} can be easily tuned without changing the morphology by making use of the epitaxial seeded growth method (Figure S5, Table S2). However, if we used $Na(Gd,Yb)F_4$:Er as the starting core of the core/shell nanostructure, the particle size of the $Na(Gd,Yb)F_4$:Er would be uncontrollable when the Yb:Er doping ratio is changed (Scheme S1, Figure S6), which results in spectral data that are not comparable because the PL properties depend on the size of the lanthanide-based NCs. The composition of the S1 layer was optimized by carefully adjusting the Yb/Er doping ratio, and $NaYbF_4$:2% Er was found to be the most efficient SWIR emitter. (Figure 2 A). Similar experiments to adjust the amount of the dopant were also carried out to optimize the Yb and Nd doping concentrations in the S2 and S3 shells (Figure 2 B, C). We found that the optimum composition for efficient SWIR emission on 800 nm excitation is $NaGdF_4/NaYbF_4$:2 Er/$NaYF_4$:10 Yb/$NaNdF_4$:10 Yb.

To study their in vitro and in vivo bioimaging performance, the SWIR NCs were transferred from the organic phase to the aqueous phase by coating amphiphilic 1,2-distearoyl-sn-glycero-3-phosphoethanolamine-*N*-[carboxy-(polyethylene glycol)-2000] (DSPE-PEG2000-COOH) phospholipids onto the surface of the SWIR NCs to form NC–phospholipid micelle complexes. The resultant hydrophilic SWIR NCs remained monodisperse in size (Figure S7) with nearly 60% of the SWIR emission intensity retained compared to the oleate-capped C/S1/S2/S3 NCs (Figure 2 D).

Before we studied the tissue penetration ability of the SWIR radiation emitted by the C/S1/S2/S3 NCs, we conducted experiments on the penetration ability through water and the overheating effects on tissues of the 800 nm light in comparison with the commonly used 980 nm laser source. The energy attenuation of the 800 nm laser was 60% weaker than that of the 980 nm laser after penetrating through water with a depth of 5 cm, suggesting that 800 nm has a strong water penetration ability. Lower absorption of the 800 nm emission by water not only results in deeper penetration, but also minimizes tissue overheating (Figure S10–12).

We next studied the penetration depth of our C/S1/S2/S3 NCs. A pellet of the NCs was excited at 800 nm, and the 1525 nm signal was imaged using an InGaAs camera through increasingly thick tissue (pork slices). Notably, SWIR signals from the C/S1/S2/S3 NCs were clearly detectable through 1.8 cm of pork tissue, which is much deeper than the depth reported for the 1525 SWIR probe excited by a 980 nm laser (1.0 cm) with a comparable excitation power density (ca. 30 μW), further confirming that the 800 nm excitation source is more suitable for in vivo applications.[7] Moghe et al. have demonstrated that 1525 nm SWIR transmits more effectively through tissue phantoms than 800 nm NIR light with the same intensity.[7] This was the first experimental demonstration of the imaging advantages of SWIR, which are due to reduced tissue scattering within this second window compared with emitters in the first NIR window. However, there are still no experimental results to evaluate the effect of the wavelength on the bioimaging performance in the second NIR window. We thus systematically evaluated the dependence of the in vitro and in vivo bioimaging performance on the SWIR emission wavelength by comparison with the previously reported $NaGdF_4$:Nd/$NaGdF_4$ NCs with a 1060 nm SWIR signal also upon 800 nm excitation (Figure 3 A,B and Figure S13). Compared to NCs designed to emit a 1525 nm signal, no signal with an appreciable signal-to-noise ratio could be observed with the $NaGdF_4$:Nd/$NaGdF_4$ NCs at a depth of 1 cm in a tissue slice. To accurately compare the penetration depth of 1525 nm to 1060 nm signals, the emission power of the RE pellet and the output power of the NIR source were matched to have identical spectral intensities prior to the application of the tissue phantoms.

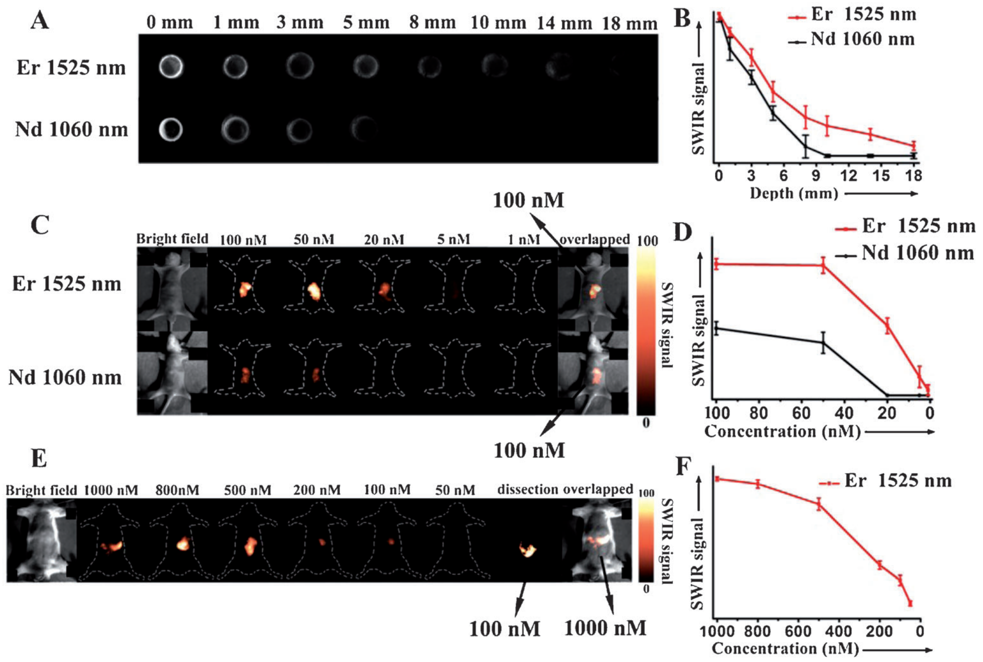

Figure 3. A,C) Comparison of the SWIR signals of C/S1/S2/S3 NCs (Er 1525 nm) and $NaGdF_4$:Nd/$NaGdF_4$ (Nd 1060 nm) in A) pork muscle tissues of various thicknesses and B) in the stomach of nude mice with different NC concentrations. E) SWIR images of the C/S1/S2/S3 NCs in the stomach of SD rats at different concentrations. B, D, F) Corresponding signal intensity curves. Note that the intensities of the two systems at 0 mm were almost the same, and appropriately equipped filters were used.

Aside from deep penetration, low detection threshold concentrations with high resolution are also an essential quality for optical biomedical imaging agents. As a proof-of-concept experiment, we imbedded different concentrations (1, 5, 20, 50, 100 nM) of the modified C/S1/S2/S3 NCs and $NaGdF_4$:Nd/$NaGdF_4$ NCs into pork muscle tissue at various depths (5, 8, and 15 mm) to investigate the bioimaging feasibility with the InGaAs camera (Figure S14). It can be seen that the SWIR signals of the C/S1/S2/S3 NCs were detectable in pork tissue at a depth of 5 mm even when the concentration was as low as 1 nM. At depths of 8 mm and 15 mm, the detection threshold increased to 20 nM and 50 nM, respectively. Nevertheless, the detection thresholds of $NaGdF_4$:Nd/$NaGdF_4$ NCs were 20 nM and 50 nM at depths of 5 mm and 8 mm, respectively, which are much higher than those of the C/S1/S2/S3 NCs. At a depth of 15 mm, only very weak signals could be detected when $NaGdF_4$:Nd/$NaGdF_4$ NCs had been imbedded.

To evaluate the capability of these modified C/S1/S2/S3 NCs for in vivo imaging, bioimaging experiments were carried out with nude mice and SD rats. First, we designed a bioimaging experiment with two groups of six-week-old nude mice. For group 1, solutions (0.2 mL) with different concentrations (1, 5, 20, 50, 100 nM) of the water-soluble C/S1/S2/S3 NCs were delivered to the stomach by using a gastric syringe. For group 2, water-soluble $NaGdF_4$:Nd/$NaGdF_4$ NCs at the same concentrations were used instead. After digestion for 20 minutes, SWIR images were taken for both groups upon 800 nm irradiation ($0.2\ W\,cm^{-2}$) with appropriately equipped filters. Bright 1525 nm SWIR signals were detected when C/S1/S2/S3 NCs were used (Figure 3 C). Moreover, for NC concentrations as low as 5 nM, the 1525 nm SWIR signals were still detectable. Considering the depth of the nude-mice stomach (3–5 mm), these results are consistent with the detection thresholds obtained during the above-mentioned experiments with pork tissue (Figure S14). By comparison, the SWIR signals from the $NaGdF_4$:Nd/$NaGdF_4$ NCs were weaker and could only be detected if the NCs were present in high concentration (> 50 nM). Therefore, we have demonstrated that the low detection threshold of the C/S1/S2/S3 NCs can be used for the in vivo imaging in small animal models. To further highlight the use of the C/S1/S2/S3 NCs for deep-penetration and high-resolution bioimaging, we chose SD rats as a bioimaging animal model. Similar gavage procedures had been performed on the SD rats using C/S1/S2/S3 NCs. Figure 3 E shows that the stomach and intestinal tract of the SD rats also exhibited bright fluorescence owing to the C/S1/S2/S3 NCs, with the detection threshold determined to be 100 nM. The outline of the stomach could be well imaged after dissection, suggesting that our images were taken in the right position. Furthermore, the depth of the SD mice stomach was determined to 0.8–1.2 cm, further demonstrating the good bioimaging performance of the C/S1/S2/S3 NCs with deep penetration and a low detection threshold.

For optical in vivo imaging, the tissue penetration depth generally depends on the absorption and scattering of the excitation and emission light. Bashkatov et al.[23] have proposed a theoretical model to calculate the penetration depth: $\delta = [3\mu_a(\mu_a+\mu_{s'})]^{-1/2}$, where μ_a is the optical absorption extinction coefficient, which depends on the wavelength (Figure S15 A), μ_s (ca. λ^{-w}) is the reduced scattering coefficient, and δ is the resulting penetration depth. The exponent (w) depends on the size and concentration of scatterers in the tissue and ranges from 0.22 to 1.68 for different tissues (Figure S15 B). From the theoretical model and our results, we can conclude that the absorption by water is stronger for 1525 nm than for 1060 nm light, but with 1060 nm light, more tissue scattering is observed than with 1525 nm light. Obviously, in our case, the reduced scattering coefficient $\mu_{s'}$ played a much more important role in determining the penetration depth δ than the absorption extinction coefficient μ_a. Therefore, we suggest that the imaging performance of SWIR is significantly influenced by the wavelength, which directly affects both μ_a and $\mu_{s'}$; moreover, the dominance of either parameter is uncertain based on simulation analysis and should depend on the application.

In conclusion, highly efficient SWIR PL under 800 nm irradiation was achieved in C/S1/S2/S3 structured lanthanide-based NCs using the epitaxial seeded growth method. After coating with phospholipids, the water-soluble NCs showed good biocompatibility and low toxicity. We also demonstrated that the obtained NCs possess great potential in SWIR bioimaging with deep penetration (18 mm) and low detection thresholds (5 nM for the stomach of nude mice and 100 nM for the stomach of SD rats). Furthermore, we confirmed that 1525 nm light is superior to 1060 nm light as the bioimaging light source in the SWIR region. We believe that further investigations are necessary to reveal how the emission wavelength influences the imaging performance of the SWIR probe and to develop novel probes with efficient SWIR emission.

Received: July 21, 2014

Keywords: bioimaging · core/shell structures · imaging agents · nanomaterials

[1] R. Wang, F. Zhang, *J. Mater. Chem. B* **2014**, *2*, 2422 – 2443.
[2] S. Adams, R. P. Baum, T. Stuckensen, K. Bitter, G. Hor, *Eur. J. Nucl. Med.* **1998**, *25*, 1255 – 1260.
[3] G. Hong, J. T. Robinson, Y. Zhang, S. Diao, A. L. Antaris, Q. Wang, H. Dai, *Angew. Chem. Int. Ed.* **2012**, *51*, 9818 – 9821; *Angew. Chem.* **2012**, *124*, 9956 – 9959.
[4] R. Weissleder, *Nat. Biotechnol.* **2001**, *19*, 316 – 317.
[5] V. J. Pansare, S. Hejazi, W. J. Faenza, R. K. Prud'homme, *Chem. Mater.* **2012**, *24*, 812 – 827.
[6] X. H. Gao, Y. Y. Cui, R. M. Levenson, L. W. K. Chung, S. M. Nie, *Nat. Biotechnol.* **2004**, *22*, 969 – 976.
[7] D. J. Naczynski, M. C. Tan, M. Zevon, B. Wall, J. Kohl, A. Kulesa, S. Chen, C. M. Roth, R. E. Riman, P. V. Moghe, *Nat. Commun.* **2013**, *4*, 2199.
[8] Y. P. Du, B. Xu, T. Fu, M. Cai, F. Li, Y. Zhang, Q. B. Wang, *J. Am. Chem. Soc.* **2010**, *132*, 1470 – 1471.
[9] K. Welsher, S. P. Sherlock, H. J. Dai, *Proc. Natl. Acad. Sci. USA* **2011**, *108*, 8943 – 8948.
[10] Z. Liu, W. Cai, L. He, N. Nakayama, K. Chen, X. Sun, X. Chen, H. Dai, *Nat. Nanotechnol.* **2006**, *2*, 47 – 52.
[11] A. L. Rogach, A. Eychmüller, S. G. Hickey, S. V. Kershaw, *Small* **2007**, *3*, 536 – 557.
[12] R. Hardman, *Environ. Health Perspect.* **2006**, *114*, 165 – 172.
[13] Z. Liu, W. Cai, L. He, N. Nakayama, K. Chen, X. Sun, X. Chen, H. Dai, *Nat. Nanotechnol.* **2006**, *2*, 47 – 52.
[14] X. M. Li, F. Zhang, D. Y. Zhao, *Nano Today* **2013**, *8*, 643 – 676.
[15] R. X. Yan, Y. D. Li, *Adv. Funct. Mater.* **2005**, *15*, 763 – 770.
[16] J. W. Stouwdam, F. van Veggel, *Nano Lett.* **2002**, *2*, 733 – 737.
[17] M. Kamimura, N. Kanayama, K. Tokuzen, K. Soga, Y. Nagasaki, *Nanoscale* **2011**, *3*, 3705 – 3713.
[18] X. Li, R. Wang, F. Zhang, L. Zhou, D. Shen, C. Yao, D. Zhao, *Sci. Rep.* **2013**, *3*, 3536.
[19] H. Wen, H. Zhu, X. Chen, T. F. Hung, B. Wang, G. Zhu, S. F. Yu, F. Wang, *Angew. Chem. Int. Ed.* **2013**, *52*, 13419 – 13423; *Angew. Chem.* **2013**, *125*, 13661 – 13665.
[20] X. Xie, N. Gao, R. Deng, Q. Sun, Q.-H. Xu, X. Liu, *J. Am. Chem. Soc.* **2013**, *135*, 12608 – 12611.
[21] Y. F. Wang, G. Y. Liu, L. D. Sun, J. W. Xiao, J. C. Zhou, C. H. Yan, *ACS Nano* **2013**, *7*, 7200 – 7206.
[22] Y. T. Zhong, G. Tian, Z. J. Gu, Y. J. Yang, L. Gu, Y. L. Zhao, Y. Ma, J. N. Yao, *Adv. Mater.* **2014**, *26*, 2831 – 2837.
[23] A. N. Bashkatov, E. A. Genina, V. I. Kochubey, V. V. Tuchin, *J. Phys. D* **2005**, *38*, 2543 – 2555.